# Sea-level fluctuations control the distribution of highly liquefaction-prone layers on volcanic-carbonate slopes

N. Sultan, G. Jouet, V. Riboulot, M. Terzariol, S. Garziglia, A. Cattaneo, J. Giraudeau, S.J. Jorry

▶ **To cite this version:**

# Sea-level fluctuations control the distribution of highly liquefaction-prone layers on volcanic-carbonate slopes

N. Sultan[1], G. Jouet[1], V. Riboulot[1], M. Terzariol[1], S. Garziglia[1], A. Cattaneo[1], J. Giraudeau[2] and S.J. Jorry[1]
[1]Geo-Ocean UMR6538, Ifremer, CNRS, UBO, UBS, 29280 Plouzané, France
[2]Environnements et Paléoenvironnements Océaniques et Continentaux (EPOC), UMR 5805, Université de Bordeaux,
 CNRS, 33615 Pessac CEDEX, France

## ABSTRACT

**Understanding and quantifying the hazards related to earthquake-induced submarine liquefaction and landslides are particularly significant offshore of tropical volcanic-carbonate islands, where carbonate production competes with volcanism to create highly contrasted lithological successions. To improve the detection of liquefaction-prone layers, we analyzed physical properties and mineralogy and performed 70 dynamic triaxial tests on 25 sediment cores offshore of the eastern side of Mayotte (Comoros archipelago in the western Indian Ocean) in an area that has experienced significant seismicity since 2018. We found that the main parameter controlling the liquefaction potential offshore of Mayotte is the presence of low-density layers with high calcite content accumulating along the slope during lowstands. This phasing with sea-level fluctuations implies a significant recurrent geohazard for tropical volcanic-carbonate islands worldwide. Furthermore, the relationship we found between the cyclic resistance of sediment and its density and magnetic susceptibility represents a time-effective approach for identifying the hazards related to earthquake-induced liquefaction.**

## INTRODUCTION

Since 2018 CE, Mayotte in the Comoros archipelago (western Indian Ocean) has faced a seismic crisis related to the birth of an ∼820-m-high submarine volcano ∼50 km offshore of the southeastern coastline (Cesca et al., 2020; Feuillet et al., 2021). As a result of the enhanced seismicity, ground shaking may weaken and destabilize the steep submarine sedimentary slopes (Audru et al., 2006) and potentially generate tsunamis (Poulain et al., 2022). In this context, understanding and quantifying hazards related to earthquake-induced submarine landslides become significant challenges. The eastern submarine slope of Mayotte would be especially vulnerable to slope failure by liquefaction because of high accumulations of carbonate and volcanic sediments on steep slopes, locally exceeding 35°. Deposition along the Mayotte slope has been modulated by the sediment supply rate, which is a function of the temporal variability of the production, the shutting down of reefal carbonate and volcanoclastic sediments (Zinke et al., 2003), and the local

morphology (Counts et al., 2018). We carried out triaxial tests to define the liquefaction potential of shallow sedimentary layers (<27 m below seafloor [mbsf]), with an aim of identifying new sedimentological and geotechnical criteria to define regional liquefaction hazard mapping.

## RESULTS

Offshore of Mayotte (north Mozambique Channel; Fig. 1A), the seafloor exhibits alignments of volcanic cones, especially east of Petite-Terre island where they form a 50-km-long ridge down to ∼3500 m below sea level (mbsl) (Fig. 1A) (Tzevahirtzian et al., 2021). In the northeast sampling area (Fig. 1B), failure scars of ∼200 m in width affect the upper slope (<1000 mbsl) while headscarps ∼700 m long run along the flanks of erosive channels in deeper waters (Fig. 1C). In the Pamanzi sampling area, mass wasting left even larger failure scars near the toe of the slope between 1200 mbsl and 1400 mbsl (Fig. 1D). Staircase geometries reminiscent of retrogressive failure are common in most of these scars. During the

French Oceanographic Cruise MAYOBS19 (Rinnert et al., 2021), 25 Calypso piston cores were collected to characterize the mineralogical, physical, and mechanical properties of the sediments (Fig. 1B).

## Density and Magnetic Susceptibility

Piston cores range between 2.25 and 26.28 m long (Table S2 in the Supplemental Material[1]). We analyzed the cores using a multi-sensor core logger (MSCL) to acquire bulk density ($\gamma$-density) and volume-specific magnetic susceptibility (MS) data. The MS and $\gamma$-density profiles obtained on the longest core CS25 (Fig. S1 in the Supplemental Material) illustrate the cyclic variability in lithological composition. For this study, $\gamma$-density and MS values were normalized with respect to the maximum and minimum values as follows:

$$\gamma_N = (\gamma - \gamma_{min})/(\gamma_{max} - \gamma_{min}), \qquad (1)$$

$$MS_N = (MS - MS_{min})/(MS_{max} - MS_{min}), \quad (2)$$

where the minimum and maximum values of $\gamma$ (1.45 and 1.83 g/cm³) and MS (2 and 782) are obtained from the 70 tested samples (Table S2).

## Dynamic Triaxial Tests

Dynamic triaxial tests were carried out on samples recovered from different lithological layers (Fig. 1). Each sample was first saturated and consolidated isotropically to a mean effective stress ($p'_0$) equivalent to (or slightly exceeding) the *in situ* effective stress (Table S2). Samples were then cyclically sheared by applying a sinusoidal differential stress ($q = \sigma_1 - \sigma_3$). Cyclic test results mainly included (Fig. S2) the cyclic resistance ratio [CRR = $q/(2p'_0)$]; the normalized mean effective stress ($p'/p'_0$);
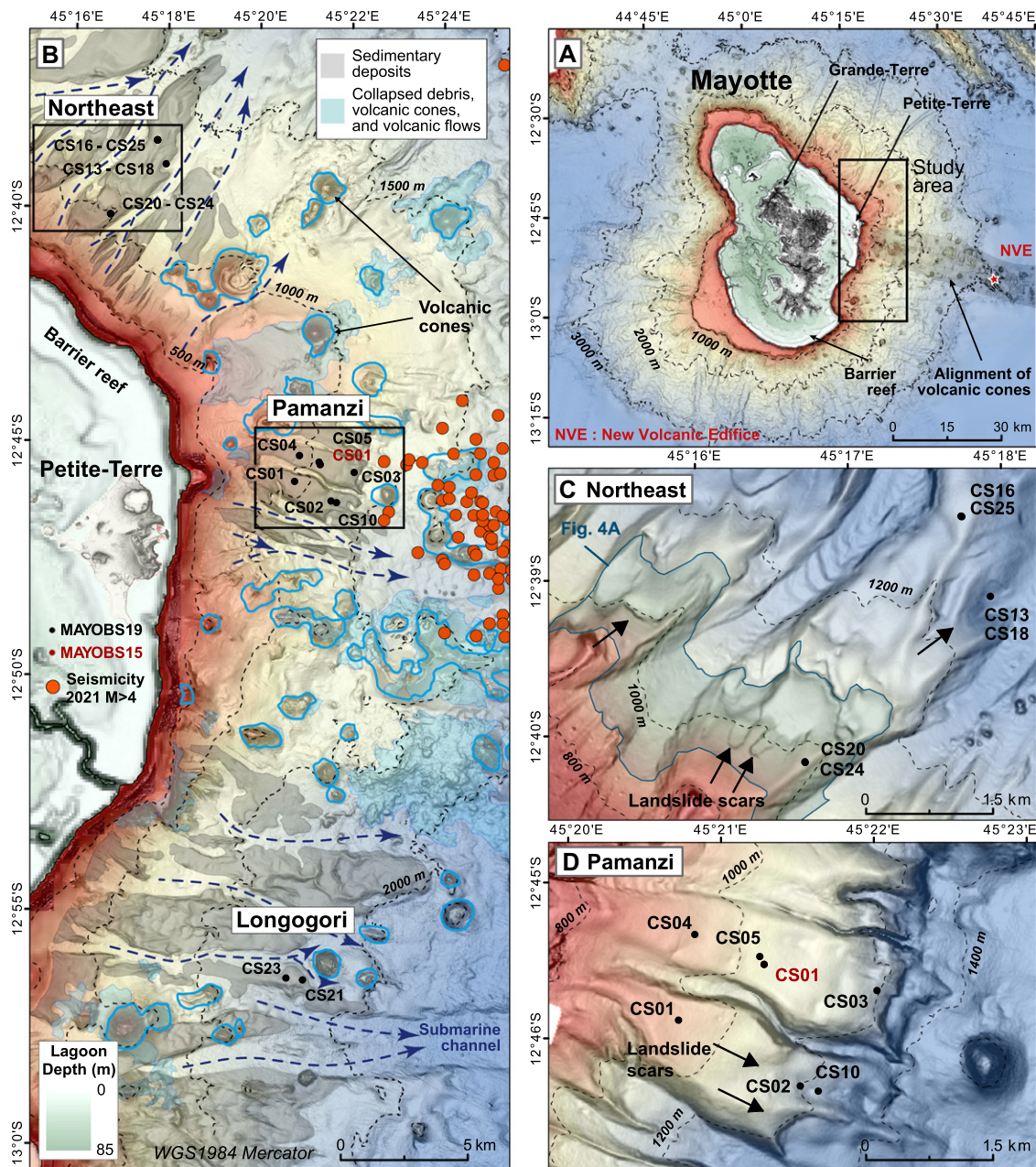
---

Figure 1. (A) General bathymetric map of Mayotte in the Comoros archipelago (western Indian Ocean). WGS—World Geodetic System. (B) Bathymetric map of the eastern slope of Mayotte (Rinnert et al., 2019) with cores from French Oceanographic Cruises MAYOBS15 and MAYOBS19 plotted as small dots. (C,D) Shaded bathymetric view with core locations in the Northeast and Pamanzi sampling areas. Maps in C and D illustrate the occurrence of submarine failure scars shaping slopes.

the shear strain ($\varepsilon_s$); and the normalized excess pore pressure ($R_u = \Delta u/\sigma'_3$) where $\Delta u$ is the excess pore pressure. We considered two different liquefaction criteria: the number of cycles $N$ equal to $N_{Ru}$ (when $R_u = 1$), or $N_{DA}$ (the number of cycles to reach a double-amplitude shear strain of 6%; Olson et al., 2020). Sixty-three (63) tests were successful (Table S2). Fifty-eight (58) samples liquefied under mean CRR values ranging between 0.13 and 0.69 and $N$ values between 3 and 100 (Table S2).

**Clay Content and Mineralogy**

The apparent correlation between $\gamma$-density and MS of the analyzed sediment samples (Fig. 2A) led us to investigate their bulk mineralogical composition from X-ray diffraction (XRD) analyses performed with a Bruker AXS diffractometer (Fig. 2B). The predominant concentrations of three carbonate types (aragonite, Mg-calcite, and calcite) are found in the lower-density sediments, while the presence of mafic minerals (i.e., clinopyroxene and plagioclase feldspar) associated with abundant ferromagnetic particles compose the high-MS sediments. The mineralogical composition allows us to determine two end members: the carbonate-dominated and the volcanic-dominated sediments. The grain-size distributions obtained with a Malvern Mastersizer 3000 indicate that carbonate sediments are slightly coarser grained (Fig. 2C). The amount of clay (<2 μm) is almost constant. Individual particles in representative sieved (>63 μm) samples from the two end members were imaged using a scan-ning electron microscope (SEM; Thermofisher Quanta 200, sputter coated with Au; Fig. 2D). Magnetic particles were separated manually with a magnet. Carbonate-dominated samples show an expected biogenic prevalence (e.g., foraminifera, mollusk shells, and echinoids), while volcanic-dominated layers show a biogenic-based matrix with magnetic particles. An inset in Figure 2D shows a typical magnetic inclusion of regular shape (euhedral, tetrahedral, or octahedral) with rounded edges.

**DISCUSSION**

**Sediment Source and Physical Properties**

Slope sedimentation offshore Mayotte comprises carbonate particles produced by the barrier reef and volcanoclastic particles derived from continental erosion and soil
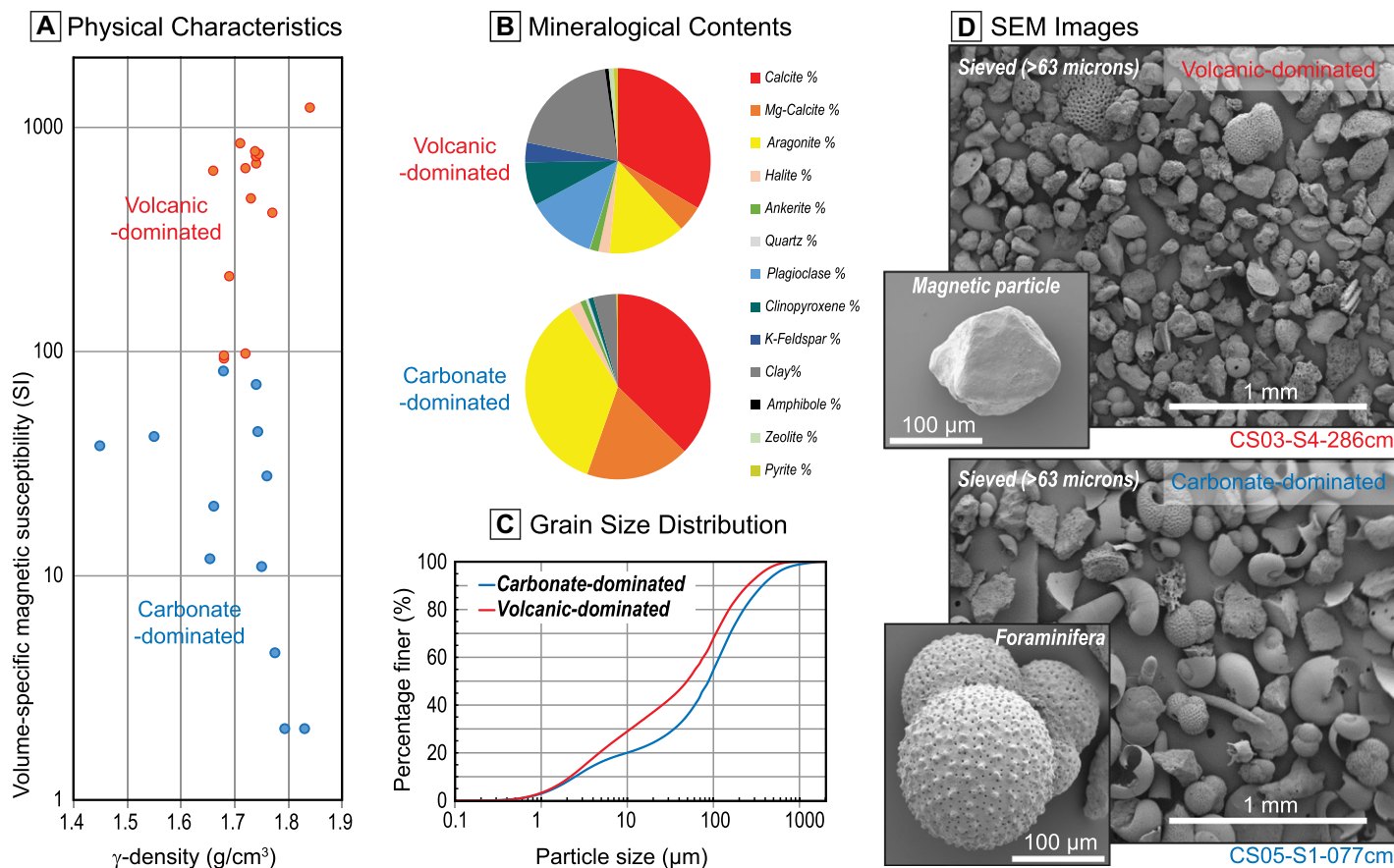
**Figure 2.** (A) Relationship between γ-density and magnetic susceptibility of the analyzed sediment samples. (B–D) Two end members, volcanic- and carbonate-dominated sediments, are identified based on their bulk mineralogical compositions determined by X-ray diffraction analysis (B), mean grain-size distribution (C), and scanning electron microscope (SEM) images (D).

denudation of exposed volcanos. The physical parameters (γ-density and MS) and mineralogical composition of the sediments reflect this partitioning between carbonate-dominated and volcanic-dominated end members (Fig. 2). The highest values in MS prevail in sediments rich in detrital and volcanic minerals (Ellwood et al., 2006) such as feldspar, plagioclase, pyroxene, and zeolites (Hunt et al., 1995). On the other hand, carbonate minerals such as calcite and Mg-carbonate are diamagnetic and present low MS values (Ellwood et al., 2000). Furthermore, the presence of carbonate-rich deposits is associated with cyclic variations of γ-density along cores (core CS25 in Fig. S1D). These γ-density fluctuations are linked mainly to the carbonate mineralogy induced by sea-level changes (Figs. S1A and S1B): aragonite (specific gravity of 2.93) and high-magnesium calcite (HMC) are produced mainly by neritic carbonates (Boardman, 1978) during highstands (when the Mayotte barrier reef is flooded), while low-magnesium calcite (LMC; specific gravity of 2.7) preferentially accumulates along the slope during lowstands and is mainly of planktic origin (Paul et al., 2012; Counts et al., 2019).

## Liquefaction in Carbonate-Rich Sediments

Results of cyclic tests outline the variation of CRR as a function of the number of cycles to liquefaction ($N_{Ru}$) (Fig. 3A). The large variability of CRR with $MS_N$ for a given $N_{Ru}$ reveals the distinct cyclic response of sediments. Considering a data subset with constant $N_{Ru}$ and $\gamma_N$, CRR varies linearly with $MS_N$ with a slope of 0.31. When a data subset with constant $N_{Ru}$ and $MS_N$ is considered, the CRR varies linearly with $\gamma_N$ with a slope of 0.25. Finally, following Idriss and Boulanger (2006), CRR was related to $N$ by a power relationship of the following form:

$$CRR = \left(0.25\gamma_N + 0.31\,MS_N + 0.39\right)N^{-0.13}. \quad (3)$$

The error between observed and calculated CRR using Equation 3 is shown in Figures 3B and 3C. It is distributed normally with a standard deviation $\sigma_d$ of 0.2. Absolute errors >0.15 occur when $N$ values are consistently >15 (dark gray in Fig. 3B), which corresponds to earthquakes of magnitudes (>7) exceeding those measured in Mayotte (Bertil et al., 2021). This good relationship between CRR and $N$ showing a strong dependence on $\gamma_N$ and $MS_N$ clearly illustrates the major role of sediment composition. Thus, based on this data set, assessment of the liquefaction

potential given an earthquake can be simplified by determining the MS and the γ-density of the sediment.

## Factor of Safety and Probability of Liquefaction

The key assumption of our method lies in the hypothesis that an earthquake of a given magnitude and site-source distance can be simulated in the laboratory by a number of uniform stress cycles (Seed and Idriss, 1971; Liu et al., 2001). This provides a convenient means for comparing the CRR to the earthquake-induced cyclic stress ratio (CSR) (Seed and Idriss, 1971; Whitman, 1971). The CSR is estimated by using a simplified equation (Equations S1–S5 in the Supplemental Material) considering the peak ground acceleration (Roullé et al., 2022). The factor of safety against liquefaction can then be calculated as follows:

$$FoS = CRR/CSR. \quad (4)$$

Figure 3D illustrates the determination of the FoS for core CS25 (additional results are shown in Figures S3–S5). The CRR values were determined for 15 cycles (earthquake scenario of $M_w = 6.75$ at 25 km distance). Under this scenario, we identified two liquefiable layers where
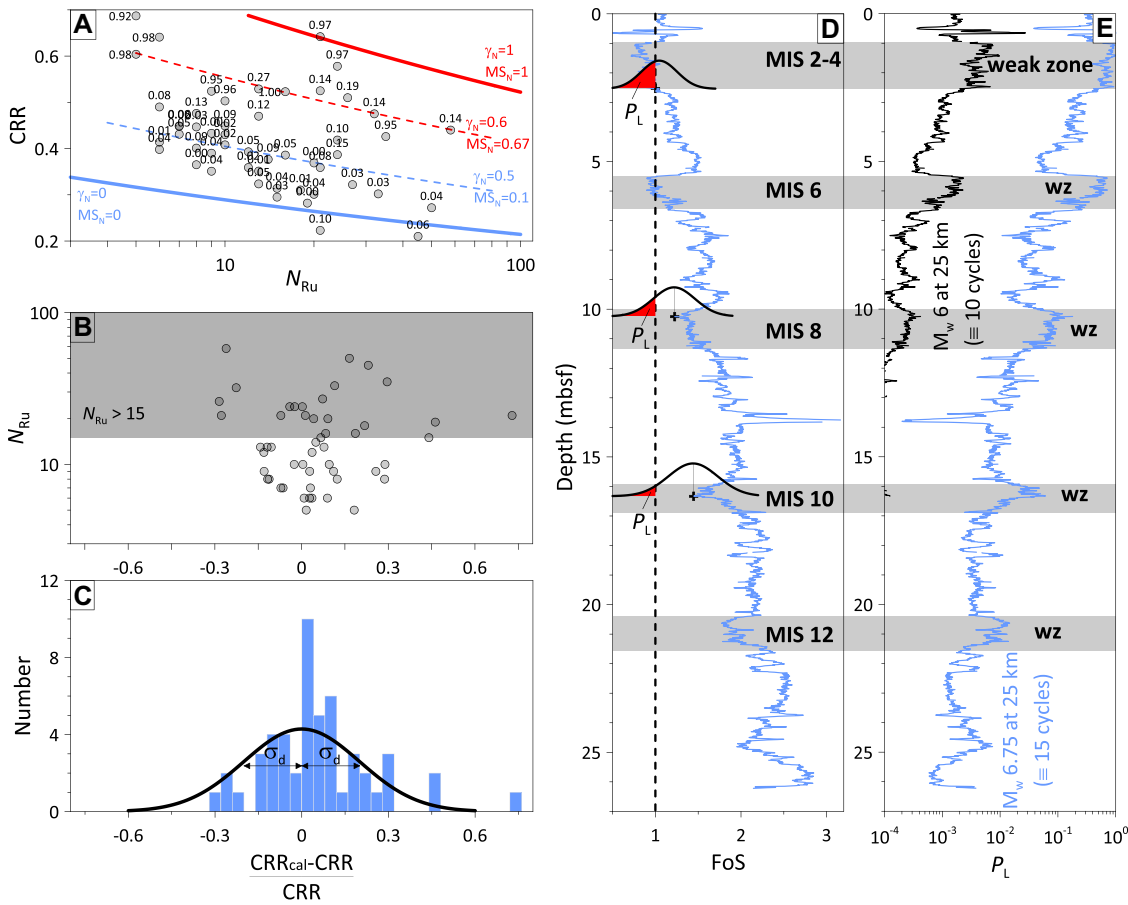
**Figure 3.** (A) Cyclic resistance ratio (CRR) as function of number of loading cycles to reach liquefaction considering the normalized excess pore pressure criteria ($N_{Ru}$). Numbers indicate the normalized magnetic susceptibility ($MS_N$) values. $\gamma_N$ corresponds to the normalized γ-density. (B) Absolute error between calculated ($CRR_{cal}$) and observed CRR is <0.15 for the majority of data. (C) Error range is distributed normally with a standard deviation, $\sigma_d$, of 0.2. Number—number of samples. (D) Factor of safety (FoS = CRR/CSR, where CSR is cyclic stress ratio) against liquefaction versus depth obtained for core CS25. CRR values are calculated for a number of cycles of 15, while earthquake-induced CSR values are determined for a hypothetical earthquake of $M_w$ 6.75 at 25 km from core. Normal distribution of FoS is also shown, where red areas corresponding to FoS < 1 are used to calculate the probability of liquefaction, $P_L$. (E) $P_L$ versus depth in core CS25 calculated for two different earthquake scenarios with $M_w$ 6 and $M_w$ 6.75. Different weak zones (wz) are pointed out in this graph, and they correspond to first order to low-γ-density layers with higher calcite content (low-magnesium calcite) accumulated during glacial lowstand periods (Marine Isotope Stages, MIS, identified in gray bars; see Fig. S1 [see footnote 1]). mbsf—meters below seafloor.

FoS < 1 (between 0.5 and 2.5 mbsf and between 5.5 and 6.25 mbsf). Furthermore, the few layers characterized by lower FoS than the general trend (noted "wz" for weak zone in Fig. 3) correspond to sediments deposited during glacial lowstand periods of reduced reef carbonate activity (Fig. S1). The lower γ-density is associated with a higher accumulation of calcite sourced from the exposed reef platform where aragonite-to-calcite diagenetic transformation occurred.

From the calculated $\sigma_d$ (0.2) shown in Figure 3C, the normal distribution of FoS and the probability of liquefaction $P_L$ were derived (Equations S6–S9; Fig. 3D). For core CS25, the FoS and $P_L$ values were calculated for two earthquake scenarios ($M_w$ 6 and $M_w$ 6.75 at 25 km from CS25). Figures 3D and 3E illustrate how the presence of high carbonate content produces several weak zones with a non-negligible liquefaction probability. Data in Figures 3D and 3E indicate that three layers (at ∼16, ∼21, and ∼25 mbsf) are characterized by a FoS > 1 but still rather low in terms of $P_L$. The $P_L$ values decrease with depth, tending to zero ($P_L < 10^{-3}$) at specific depths below the seabed (>22.5 mbsf for $M_w$ 6.75 and >2.5 mbsf for $M_w$ 6; Fig. 3E).

The recurrent weak zones in the stratigraphic record in Figure 3E are associated with the 100 k.y. glacial-interglacial cyclicity of sea-level fluctuations during the late Quaternary. Weak zones are related to periods of low sea level when the Mayotte barrier reef was subaerially exposed and the aragonite and HMC input was minimum. Sediments in weak zones are characterized by lower density due to the preferential LMC deposition.

**Probability of Liquefaction versus Geometric Characteristics of Observed Landslides**

Three landslides located between 0.5 and 4 km from core CS24 are shown in Figure 4A. Based on the four cross sections (a, b, c, and d) presented in Figure 4B, the initial seabed geometry was reconstructed (Fig. 4B). The three landslides are characterized by flat failure surfaces parallel to the seabed (Fig. 4B) and low slope angles not exceeding 2°. These features can be ascribed to the development of a failure surface along a weak stratigraphic horizon (Locat et al., 2014). The physical properties and probability of liquefaction for an earthquake of $M_w$ 6.75 point out three weak layers in terms of liquefac-

tion at 9–10 mbsf, 14–15 mbsf, and 16–17 mbsf (gray rectangles in Fig. 4C). The intermediate weak layer is surrounded by two stiff layers, and its depth below the seabed fits with the mean depths of the three landslides shown in Figure 4B. By considering constant sedimentation in the area, it is plausible to ascribe the flat failure surfaces shown in Figure 4B to the triggering of liquefaction of the layers between 9–10 mbsf and 14–15 mbsf. The presence of a weak layer between two stiff layers is an additional factor promoting liquefaction failure between 14 and 15 mbsf (Fig. 4C). Data presented in Figure 4 validate the approach here presented by confirming that liquefaction in carbonate-rich sediments is controlled primarily by the presence of low-density LMC-dominated layers formed during lowstands.

**Beyond the Case of the Mayotte Slope—Volcanic Islands, Earthquakes, and Liquefaction**

Submarine failures and landslides have been observed in many locations worldwide on the flanks of carbonate platforms and contribute to the stratigraphic evolution and major geohazard on the surrounding slopes (Janson
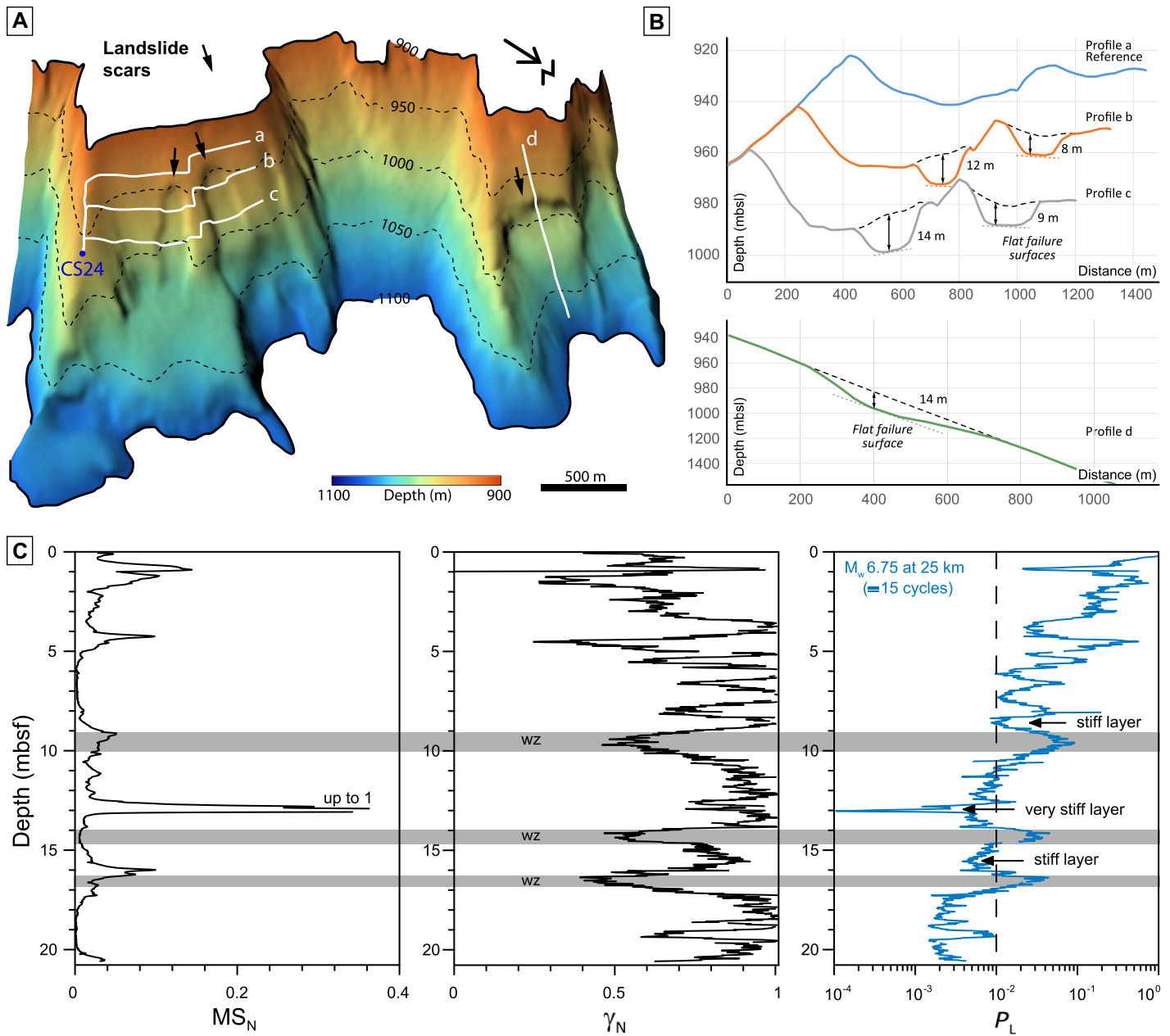
**Figure 4. (A)** Three-dimensional view focusing on three shallow landslides (see Fig. 1C for location) with positions of four cross sections (a, b, c, and d). **(B)** Bathymetric cross sections allow determination of the landslides' thicknesses (indicated with double-headed arrows), which are between 8 and 14 m. **(C)** Physical properties including the normalized γ-density ($\gamma_N$) and the normalized magnetic susceptibility ($MS_N$) and probability of liquefaction ($P_L$) for an earthquake of $M_w$ 6.75 located 25 km from core CS24 allow identifying three weak zones (wz) in terms of liquefaction at 9–10 m, 14–15 m, and 16–17 m below seafloor (gray rectangles) fitting with the depth of observed slope failures.

et al., 2010; Harbitz et al., 2012; Mulder et al., 2012, 2017; Lehrmann et al., 2020). Even if the impact of tectonic and volcanic activity on carbonate platform development remains poorly understood, many shallow-water carbonate platforms developed in the tropical realm on active or dormant volcanos throughout the Cenozoic (Courgeon et al., 2017). As a result, coeval carbonate-volcanic sedimentation is commonly reported on seamount slopes and adjacent basins (Counts et al., 2018) while the mixing of sediment fluxes depends on the volcanic activity, relief dismantling, and environmental conditions that allow reef carbonate

fabric production. The alternating deposition of such sediments on very steep slopes may therefore act as a preconditioning factor underlying repeated slope failures offshore carbonate platforms.

In the case of carbonate-rich sedimentation, either on isolated carbonate platforms (Paul et al., 2012; Counts et al., 2019; Jorry et al., 2020) or on mixed carbonate-siliciclastic margins (Droxler and Jorry, 2013; Mallarino et al., 2021), the failure mechanism is linked mainly to the depositional architecture of the carbonate system. Sedimentary systems supplied alternating aragonite and HMC versus

LMC deposits in phase with the interglacial highstand and glacial lowstand periods during the late Quaternary. Consequently, the liquefiable sediment layers along the Mayotte submarine slope originate from these mineralogical changes. Because of the cyclicity of this climate-related sedimentation, our findings point out that instabilities on carbonate slopes may represent a substantial, recurrent geohazard offshore coral reefs especially in seismic and/or volcanic zones such as the Caribbean (e.g., the Northern Nicaragua Rise), the Pacific Ocean (e.g., Hawaii), or the Indian Ocean (e.g., Indonesia).

## REFERENCES CITED

Audru, J.-C., Guennoc, P., Thinon, I., and Abellard, O., 2006, BATHYMAY: Underwater structure of Mayotte Island revealed by multibeam bathymetry: Comptes Rendus Geoscience, v. 338, p. 1240–1249, https://doi.org/10.1016/j.crte.2006.07.010.

Bertil, D., Mercury, N., Doubre, C., Lemoine, A., and Van der Woerd, J., 2021, The unexpected Mayotte 2018–2020 seismic sequence: A reappraisal of the regional seismicity of the Comoros: Comptes Rendus Geoscience, v. 353, p. 1–25.

Boardman, M.R., 1978, Holocene deposition in Northwest Providence Channel, Bahamas: A geochemical approach [Ph.D. thesis]: Chapel Hill, University of North Carolina, 155 p.

Cesca, S., et al., 2020, Drainage of a deep magma reservoir near Mayotte inferred from seismicity and deformation: Nature Geoscience, v. 13, p. 87–93, https://doi.org/10.1038/s41561-019-0505-5.

Counts, J.W., Jorry, S.J., Leroux, E., Miramontes, E., and Jouet, G., 2018, Sedimentation adjacent to atolls and volcano-cored carbonate platforms in the Mozambique Channel (SW Indian Ocean): Marine Geology, v. 404, p. 41–59, https://doi.org/10.1016/j.margeo.2018.07.003.

Counts, J.W., Jorry, S.J., Vazquez Riveiros, N., Jouet, G., Giraudeau, J., Chéron, S., Boissier, A., and Miramontes, E., 2019, A Late Quaternary record of highstand shedding from an isolated carbonate platform (Juan de Nova, southern Indian Ocean): The Depositional Record, v. 5, p. 540–557, https://doi.org/10.1002/dep2.57.

Courgeon, S., et al., 2017, Impact of tectonic and volcanism on the Neogene evolution of isolated carbonate platforms (SW Indian Ocean): Sedimentary Geology, v. 355, p. 114–131, https://doi.org/10.1016/j.sedgeo.2017.04.008.

Droxler, A.W., and Jorry, S.J., 2013, Deglacial origin of barrier reefs along low-latitude mixed siliciclastic and carbonate continental shelf edges: Annual Review of Marine Science, v. 5, p. 165–190, https://doi.org/10.1146/annurev-marine-121211-172234.

Ellwood, B.B., Crick, R.E., El Hassani, A., Benoist, S.L., and Young, R.H., 2000, Magnetosusceptibility event and cyclostratigraphy method applied to marine rocks: Detrital input versus carbonate productivity: Geology, v. 28, p. 1135–1138, https://doi.org/10.1130/0091-7613(2000)28<1135:MEACMA>2.0.CO;2.

Ellwood, B.B., Balsam, W.L., and Roberts, H.H., 2006, Gulf of Mexico sediment sources and sediment transport trends from magnetic susceptibility measurements of surface samples: Marine Geology, v. 230, p. 237–248, https://doi.org/10.1016/j.margeo.2006.05.008.

Feuillet, N., et al., 2021, Birth of a large volcanic edifice offshore Mayotte via lithosphere-scale dyke intrusion: Nature Geoscience, v. 14, p. 787–795, https://doi.org/10.1038/s41561-021-00809-x.

Harbitz, C.B., Glimsdal, S., Bazin, S., Zamora, N., Løvholt, F., Bungum, H., Smebye, H., Gauer, P., and Kjekstad, O., 2012, Tsunami hazard in the Caribbean: Regional exposure derived from credible worst case scenarios: Continental Shelf Research, v. 38, p. 1–23, https://doi.org/10.1016/j.csr.2012.02.006.

Hunt, C.P., Moskowitz, B.M., and Banerjee, S.K., 1995, Magnetic properties of rock and minerals, in Ahrens, T.J., ed., Rock Physics and Phase Relations: A Handbook of Physical Constants: American Geophysical Union Reference Shelf Series 3, p. 189–203.

Idriss, I.M., and Boulanger, R.W., 2006, Semi-empirical procedures for evaluating liquefaction potential during earthquakes: Soil Dynamics and Earthquake Engineering, v. 26, p. 115–130, https://doi.org/10.1016/j.soildyn.2004.11.023.

Janson, X., Eberli, G.P., Lomando, A.J., and Bonnaffé, F., 2010, Seismic characterization of large-scale platform-margin collapse along the Zhujiang carbonate platform (Miocene) of the South China Sea, based on Miocene outcrop analogs from Mut Basin, Turkey, in Morgan, W.A., et al., eds., Cenozoic Carbonate Systems of Australasia: SEPM (Society for Sedimentary Geology) Special Publication 95, p. 73–92, https://doi.org/10.2110/sepmsp.095.079.

Jorry, S.J., Jouet, G., Edinger, E.N., Toucanne, S., Counts, J.W., Miramontes, E., Courgeon, S., Vásquez Riveiros, N., Le Roy, P., and Camoin, G.F., 2020, From platform top to adjacent deep sea: New source-to-sink insights in carbonate sediment production and transfer in the SW Indian Ocean (Glorieuses archipelago): Marine Geology, v. 423, 106144, https://doi.org/10.1016/j.margeo.2020.106144.

Lehrmann, D.J., Minzoni, M., Enos, P., Kelleher, C., Stepchinski, L., Li, X.W., Payne, J.L., and Yu, M.Y., 2020, Giant sector-collapse structures (scalloped margins) of the Yangtze Platform and Great Bank of Guizhou, China: Implications for genesis of collapsed carbonate platform margin systems: Sedimentology, v. 67, p. 3167–3198, https://doi.org/10.1111/sed.12740.

Liu, A.H., Stewart, J.P., Abrahamson, N.A., and Moriwaki, Y., 2001, Equivalent number of uniform stress cycles for soil liquefaction analysis: Journal of Geotechnical and Geoenvironmental Engineering, v. 127, p. 1017–1026, https://doi.org/10.1061/(ASCE)1090-0241(2001)127:12(1017).

Locat, J., Leroueil, S., Locat, A., and Lee, H., 2014, Weak layers: Their definition and classification from a geotechnical perspective, in Krastel, S., et al., eds., Submarine Mass Movements and Their Consequences: Cham, Switzerland, Springer, p. 3–12, https://doi.org/10.1007/978-3-319-00972-8_1.

Mallarino, G., Francis, J.M., Jorry, S.J., Daniell, J.J., Droxler, A.W., Dickens, G.R., Beaufort, L., Bentley, S.J., Opdyke, B.N., and Peterson, L.C., 2021, Timescale dependent sedimentary record during the past 130 kyr from a tropical mixed siliciclastic–carbonate shelf edge and slope: Ashmore Trough (southern Gulf of Papua): Sedimentology, v. 68, p. 2606–2648, https://doi.org/10.1111/sed.12867.

Mulder, T., et al., 2012, Canyon morphology on a modern carbonate slope of the Bahamas: Evidence of regional tectonic tilting: Geology, v. 40, p. 771–774, https://doi.org/10.1130/G33327.1.

Mulder, T., et al., 2017, Carbonate slope morphology revealing sediment transfer from bank-to-slope (Little Bahama Bank, Bahamas): Marine and Petroleum Geology, v. 83, p. 26–34, https://doi.org/10.1016/j.marpetgeo.2017.03.002.

Olson, S.M., Mei, X., and Hashash, Y.M.A., 2020, Nonlinear site response analysis with pore-water pressure generation for liquefaction triggering evaluation: Journal of Geotechnical and Geoenvironmental Engineering, v. 146, 04019128, https://doi.org/10.1061/(ASCE)GT.1943-5606.0002191.

Paul, A., Reijmer, J.J.G., Fürstenau, J., Kinkel, H., and Betzler, C., 2012, Relationship between Late Pleistocene sea-level variations, carbonate platform morphology and aragonite production (Maldives, Indian Ocean): Sedimentology, v. 59, p. 1640–1658, https://doi.org/10.1111/j.1365-3091.2011.01319.x.

Poulain, P., Le Friant, A., Pedreros, R., Mangeney, A., Filippini, A.G., Grandjean, G., Lemoine, A., Fernández-Nieto, E.D., Castro Díaz, M.J., and Peruzzetto, M., 2022, Numerical simulation of submarine landslides and generated tsunamis: Application to the on-going Mayotte seismo-volcanic crisis: Comptes Rendus Geoscience, v. 354, https://doi.org/10.5802/crgeos.138 (in press).

Rinnert, E., Lebas, E., Jorry, S., Feuillet, N., Thinon, I., and Fouquet, Y., 2019, MAYOBS: https://doi.org/10.18142/291 (accessed December 2022).

Rinnert, E., Paquet, F., and Lebas, E., 2021, MAYOBS19 cruise, RV Pourquoi pas ?: https://doi.org/10.17600/18001985 (accessed December 2022).

Roullé, A., Baillet, M., Bertil, D., and Cornou, C., 2022, Site effects observations and mapping on the weathered volcanic formations of Mayotte Island: Comptes Rendus Geoscience, v. 354, https://doi.org/10.5802/crgeos.151 (in press).

Seed, H.B., and Idriss, I.M., 1971, Simplified procedure for evaluating soil liquefaction potential: Journal of the Soil Mechanics and Foundations Division, v. 97, p. 1249–1273, https://doi.org/10.1061/JSFEAQ.0001662.

Tzevahirtzian, A., Zaragosi, S., Bachèlery, P., Biscara, L., and Marchès, E., 2021, Submarine morphology of the Comoros volcanic archipelago: Marine Geology, v. 432, 106383, https://doi.org/10.1016/j.margeo.2020.106383.

Whitman, R.V., 1971, Resistance of soil to liquefaction and settlement: Soil and Foundation, v. 11, p. 59–68, https://doi.org/10.3208/sandf1960.11.4_59.

Zinke, J., Reijmer, J.J.G., Thomassin, B.A., Dullo, W.C., Grootes, P.M., and Erlenkeuser, H., 2003, Postglacial flooding history of Mayotte lagoon (Comoro Archipelago, southwest Indian Ocean): Marine Geology, v. 194, p. 181–196, https://doi.org/10.1016/S0025-3227(02)00705-3.